Quadrant Distribution of Tropical Cyclone Inner-Core Kinematics in Relation to Environmental Shear

JENNIFER C. DEHART AND ROBERT A. HOUZE JR.

University of Washington, Seattle, Washington

ROBERT F. ROGERS

Hurricane Research Division, Atlantic Oceanographic and Meteorological Laboratory, Miami, Florida

(Manuscript received 19 September 2013, in final form 17 January 2014)

ABSTRACT

Airborne Doppler radar data collected in tropical cyclones by National Oceanic and Atmospheric Administration WP-3D aircraft over an 8-yr period (2003–10) are used to statistically analyze the vertical structure of tropical cyclone eyewalls with reference to the deep-layer shear. Convective evolution within the inner core conforms to patterns shown by previous studies: convection initiates downshear right, intensifies downshear left, and weakens upshear. Analysis of the vertical distribution of radar reflectivity and vertical air motion indicates the development of upper-level downdrafts in conjunction with strong convection downshear left and a maximum in frequency upshear left. Intense updrafts and downdrafts both conform to the shear asymmetry pattern. While strong updrafts occur in the eyewall, intense downdrafts show far more radial variability, particularly in the upshear-left quadrant, though they concentrate along the eyewall edges. Strong updrafts are collocated with low-level inflow and upper-level outflow superimposed on the background flow. In contrast, strong downdrafts occur in association with low-level outflow and upper-level inflow.

1. Introduction

Although tropical cyclone vertical motion in the inner core is often approximated as axisymmetric, real cyclones are often characterized by prominent asymmetries. A better understanding of the internal structure, particularly deviations from the mean slantwise-neutral circulation, is crucial to storm-intensity forecast error improvement, which currently lags behind track forecast error (DeMaria et al. 2005). Asymmetries can arise from a variety of sources; however, the vertical wind shear of the surrounding environment has been a focus of recent studies.

Beyond its detrimental effect on tropical cyclone intensity, vertical wind shear has a crucial role in organizing the inner-core structure. Recent studies have focused attention on two mechanisms proposed to cause vertical motion asymmetries: vortex tilt and storm-relative flow.

In response to the shear-induced deep-layer tilt of the vortex, an asymmetric vertical circulation develops temporarily, where upward motion occurs downtilt and downward motion occurs uptilt, simultaneously producing a wavenumber-1 asymmetry of potential temperature. This in turn induces a second, persistent vertical motion asymmetry as air moves through the temperature anomalies (upward from the positive to negative anomalies and downward from the negative to positive anomalies). The vertical motion is 90° out of phase with the temperature anomalies (Jones 1995; Frank and Ritchie 1999; Braun et al. 2006; Reasor and Eastin 2012). In addition, vertical shear imposes opposite flow patterns onto the vortex at low and high levels: downshear, the relative flow is radially inward closer to the surface and radially outward aloft (the opposite pattern occurs upshear). Because of the strong radial vorticity gradient, this relative flow causes appreciable vorticity advection, which is approximately balanced by vortex stretching or compression (Bender 1997; Frank and Ritchie 1999, 2001; Rogers et al. 2003; Braun et al. 2006; Wu et al. 2006). Distinguishing between these two mechanisms is challenging, as the two often exist simultaneously.

Corresponding author address: Jennifer DeHart, University of Washington, 408 Atmospheric Sciences–Geophysics (ATG) Building, Box 351640, Seattle, WA 98195-1640.
E-mail: jcdehart@uw.edu

Despite the difficulty in evaluating the dominant mechanism, several observational studies have investigated the resulting impact on storm structure. However, they tend to be case studies (Black et al. 2002; Reasor et al. 2009; Reasor and Eastin 2012) or focus on horizontal patterns of vertically integrated convective proxies (Corbosiero and Molinari 2002, 2003; Chen et al. 2006). Nonetheless, a basic vertical velocity pattern emerges, wherein updrafts are more frequent downshear and downdrafts upshear. Black et al. (2002) used case studies to deduce that convective echoes initiate downshear and mature as they move around the eyewall and that reflectivity maximizes left of shear. Though not examined specifically in reference to the environmental shear, Heymsfield et al. (2001) noted a similar evolution of individual convective cells within Hurricane Bonnie. Corbosiero and Molinari (2002) and Chen et al. (2006) examined the horizontal distribution of lightning and rainfall, respectively. Within the inner core, these proxies for convection skewed preferentially toward the downshear side of the storm, with a maximum downshear left. Moreover, Corbosiero and Molinari (2003) and Chen et al. (2006) showed that when shear was stronger than a certain threshold, it was the dominant mechanism in organizing convection, superseding any effect by storm motion.

Although the asymmetric eyewall kinematic structure is often generalized by a downshear–upshear difference, both observational and modeling studies have shown that these gross asymmetries occur because of temporal and spatial averaging of smaller, transient features that evolve while circling the eyewall (Black et al. 2002; Braun et al. 2006). Using case studies of Hurricanes Jimena (1991) and Olivia (1994), Black et al. (2002) found that the convective pulses tended to be periodic. In a numerical simulation of Hurricane Bonnie, Braun et al. (2006) showed that updraft initiation could result from the interaction of smaller-scale eyewall mesovortices with low-level inflow downshear. Thus, while the vertical shear projects strongly onto the low-wavenumber structure, resolving smaller-scale features is also important.

Finally, the vertical dimension of this problem cannot be ignored. Two recent studies have used a large sample of storms to document the vertical structure of the tropical cyclone's inner core. Hence and Houze (2011) performed a statistical analysis of data obtained by the Tropical Rainfall Measurement Mission (TRMM) Precipitation Radar (PR) to investigate the vertical structure of hydrometeors in tropical cyclone eyewalls in relation to the large-scale shear. Their reflectivity distributions imply a systematic progression cyclonically from young convection in the downshear-right quadrant, to a mixture of mature convection and stratiform rain, to progressively more stratiform characteristics

around the eyewall in the upshear quadrants. Similarly, Reasor et al. (2013) took advantage of a multiyear sample of National Oceanic and Atmospheric Administration (NOAA) WP-3D tail Doppler radar data to investigate the impact of shear on the mean kinematic vertical structure. They showed that composite vertical motion was consistent with previous studies; however, they noted that peak composite motion skewed toward the quadrant with the strongest and deepest low-level inflow, that is, downshear right. By separating the storms into low- and high-shear cases, they demonstrated the robust nature of this relationship, where the high-shear cases were far more asymmetric than those storms embedded within weaker shear.

In this study, we expand upon the results of Hence and Houze (2011) and Reasor et al. (2013). We utilize the same overall dataset as Reasor et al. (2013), which provides the kinematic information that Hence and Houze (2011) lacked. However, we employ a similar statistical analysis as Hence and Houze (2011) to investigate the eyewall distribution of reflectivity and vertical velocity, as opposed to the mean, to get a better sense of the total sample variability. As in these previous studies, we examine the radar data in relation to the deep-layer large-scale environmental wind shear. Results are organized by quadrant relative to the large-scale shear vector. Using a statistical distribution approach similar to Hence and Houze (2011), but on a dataset that includes vertical air motions, allows us to determine the nature of the smaller-scale convection active in each quadrant of the storm and not simply the mean structures. Finally, we place the updraft and downdraft outliers within the context of their respective circulations to determine if they exhibit different mean dynamical characteristics. In summary, we do not focus on the net amount of mass flux or total precipitation in each quadrant, but rather seek insight into the type of small-scale cloud and precipitation features that contribute to the net fluxes and rainfall.

2. Data and methodology

This study utilizes the database of tail Doppler radar data from NOAA WP-3D aircraft from 2003 through 2010, which has been analyzed in several other studies (Rogers et al. 2012; Reasor et al. 2013; Rogers et al. 2013). Our study compiles information from 125 eyewall penetrations obtained during 39 separate flights within 12 tropical cyclones. Details regarding each flight are described in Table 1. All of the storms included in this study were of hurricane strength at the time that they were sampled; using the nearest National Hurricane Center (NHC) best-track data to the actual flight time, the average storm intensity was $56.8\,\mathrm{m\,s^{-1}}$, though the distribution is skewed toward more intense cyclones.

TABLE 1. Database characteristics.

Storm	Flight date	No. of swaths	Center time of first pass (UTC)	Center time of last pass (UTC)	850–200-hPa SHIPS-derived shear (m s^{-1})	850–200-hPa SHIPS-derived shear heading (°)	Nearest best-track intensity (m s^{-1})
Fabian	3 Sep 2003	5	1850	2244	6.8	30	56.6
	4 Sep 2003	3	2003	2233	7	340	59.2
Isabel	12 Sep 2003	2	1708	1901	8.2	192	72
Frances	30 Aug 2004	3	1812	2116	5.7	319	56.6
	31 Aug 2004	2	1721	1923	4	276	64.3
	2 Sep 2004	2	1906	2111	5.9	89	59.2
Ivan	7 Sep 2004	4	1553	1928	8.2	50	54
	9 Sep 2004	3	1642	1843	2.4	335	66.9
	12 Sep 2004	3	1130	1452	5.9	92	69.4
	13 Sep 2004	4	1826	2017	9	109	72
	13 Sep 2004	2	2150	2352	5.5	74	72
	14 Sep 2004	4	1920	2233	9	72	61.7
	14 Sep 2004	6	2046	2708	9.7	57	61.7
Katrina	27 Aug 2005	3	1651	2008	2.1	230	51.4
	28 Aug 2005	4	1755	2231	1.2	209	77.2
	29 Aug 2005	4	916	1232	5.2	81	56.6
Ophelia	11 Sep 2005	2	1638	1800	6.2	79	33.4
Rita	20 May 2005	3	1601	1815	5.6	251	43.7
	21 May 2005	3	1518	1938	2.2	346	74.6
	22 May 2005	4	1448	1913	5.3	325	64.3
	23 May 2005	4	1746	2147	7.2	21	56.6
Felix	1 Sep 2007	2	2125	2241	3.4	214	33.4
	3 Sep 2007	2	1107	1227	2.8	152	72
Gustav	29 Aug 2008	1	2402	2449	4.4	33	38.6
	30 Aug 2008	2	2147	2428	7.9	17	61.7
	30 Aug 2008	2	1001	1223	9.7	46	56.6
	31 Aug 2008	6	2058	2602	6.5	21	48.9
	31 Aug 2008	2	952	1348	9.8	13	51.4
Paloma	7 Nov 2008	3	554	839	3	51	33.4
	7 Nov 2008	5	1708	2013	5.6	55	41.2
	8 Nov 2008	5	1628	1917	15.1	39	64.3
Bill	18 Aug 2009	3	2153	2602	3.8	125	54
	19 Aug 2009	3	2159	2431	7.3	72	59.2
Earl	29 Aug 2010	4	2057	2438	4.6	205	43.7
	30 Aug 2010	3	1110	1341	3.1	122	54
	30 Aug 2010	3	2112	2334	5.9	153	59.2
	1 Sep 2010	2	1056	1217	9.4	355	56.6
	2 Sep 2010	3	935	1213	8.1	2	59.2
	2 Sep 2010	4	2204	2548	7.2	2	46.3

The data come from the X-band dual-Doppler tail radar that scans in a cone alternating 20° fore and aft of the vector normal to the airplane track as it traverses the eyewall. An automated variational algorithm (Gamache 1997) takes the measured reflectivity and Doppler radial velocity to produce gridded three-dimensional analyses. The algorithm simultaneously solves the continuity and Doppler projection equations using least squares minimization (Reasor et al. 2009). The resulting analyses, referred to as swaths, have horizontal and vertical resolutions of 2 and 0.5 km, respectively. Compared with high-resolution case studies by Black et al. (1996) and Heymsfield et al. (2010), the resolution is considerably lower; their datasets have horizontal resolutions of 750

and 100 m and vertical resolutions of 300 and 37.5 m, respectively. As a result, smoothing of the smallest features occurs in our study. While the reduced resolution is a disadvantage of the automated processing algorithm, it also enables us to analyze a large number of storms to look for common features. Therefore, despite the trade-off between sample size and resolution, we still feel that we are able to examine features smaller than quadrant means.

For each swath, we calculated the approximate storm motion from NHC best-track data, which is removed from the horizontal wind field. Next, the storm center was calculated at 2-km altitude by using a simplex algorithm (Nelder and Mead 1965), which locates the

center that maximizes the axisymmetric tangential wind within a 5-km-wide annulus. Data at all altitudes are centered relative to this location. To account for the variety of storm size, we normalize the horizontal distance of each swath by its respective radius of maximum wind at the 2-km level, as in Rogers et al. (2012). To isolate the eyewall, we define the eyewall by those pixels with normalized radius values between 0.75 and 1.25, as in Rogers et al. (2012). To analyze the characteristics of smaller-scale features, we only consider the individual radial passes; we do not merge them together, as is done in Reasor et al. (2013).

To categorize the storms by shear, we take the 850–200-hPa deep-layer shear from the Statistical Hurricane Intensity Prediction Scheme (SHIPS) database (DeMaria et al. 2005). Within our sample, the average magnitude of the vector wind difference between the two levels was $6\,m\,s^{-1}$, as seen in Table 1. Ensuring the presence of shear, we only include storms where the magnitude of the wind velocity difference between the two levels was greater than $2.5\,m\,s^{-1}$, as in Reasor et al. (2013). We then use this vector to separate the data into four shear-oriented quadrants: downshear right (DR), downshear left (DL), upshear left (UL), and upshear right (UR).

3. Eyewall statistics

To establish consistency with the conclusions of Hence and Houze (2011), we first carry out a similar analysis of reflectivity to see if the same progression of convective life cycle stage with azimuth appears in this dataset. Since the TRMM PR and NOAA P3 radar have different wavelengths (Ku and X band, respectively), sensitivities, and scanning strategies, comparing their respective eyewall reflectivity patterns is essential. Both experience attenuation, although it is more extreme for the TRMM PR and is corrected. Additionally, the datasets do not sample identical storms, although there is a great deal of overlap. After establishing that the NOAA P3 radar captures the same eyewall convective evolution with regard to radar reflectivity (i.e., the precipitation field) as TRMM, we will extend the analysis to eyewall vertical velocity derived from the airborne radar. Because of a reduction in data quality at higher altitudes, we only examine vertical velocity data below 10 km and the primary reflectivity analysis focuses on that altitude range as well.

In our analysis of tropical cyclone vertical structure, we employ contoured frequency by altitude diagrams (CFADs; Yuter and Houze 1995) of reflectivity and vertical velocity to investigate the statistical behavior of convection within hurricanes. CFADs are joint probability distributions that detail the vertical structure of
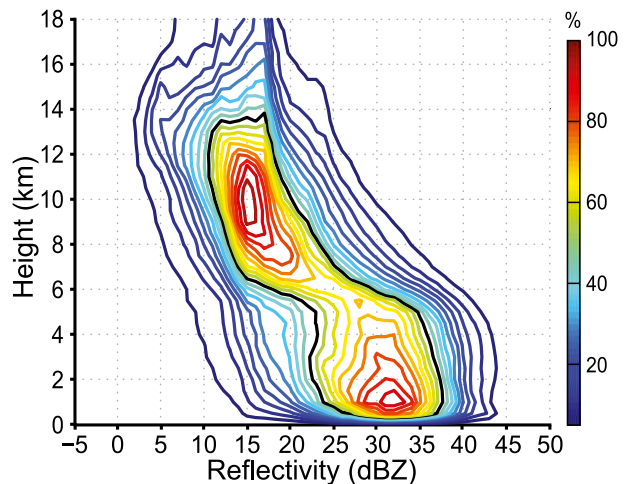

FIG. 1. CFAD of eyewall radar reflectivity binned every 1 dBZ. Contours every 5% beginning at 5% represent the frequency of occurrence relative to the maximum absolute frequency in the data sample represented in the CFAD. The 50% contour line has been colored black for reference.

data frequency. They are normalized by the maximum frequency to determine the relative contributions to bulk structure. Frequencies greater and less than 50% are hereafter referred to as the modal and outlier distributions, respectively.

a. Reflectivity

Figure 1 shows the full eyewall reflectivity structure. Two frequency peaks are evident: one associated with intense low-level rainfall and a stronger one associated with upper-level frozen hydrometeors. Altitudes below 6 km are marked by a large spread of reflectivities (~35 dB); however, the modal distribution encompasses stronger reflectivities, reflecting the intense precipitation that is characteristic of tropical cyclones. Reflectivity values decrease dramatically from 5 to 6 km, both in the modal and outlier distributions, arising from the transition from liquid to ice hydrometeors above the melting level. The frequency peak above 6 km is sharper. The brightband structure and upper-level frequency peak are consistent with the results from Hence and Houze (2011); however, their upper-level peak was much larger relative to lower levels. This difference could be related to the different sampling strategies and sensitivities of the two radars. Whereas TRMM samples from above the storms, the NOAA WP-3D aircraft typically fly at 3-km altitude. Thus, both radars suffer from attenuation, but in different directions. Additionally, the TRMM PR sensitivity is only 17 dBZ; in contrast, the NOAA radars are capable of measuring much weaker reflectivities. Thus, the upper-level signature in Fig. 1 is much broader, spanning a larger range of reflectivity values, possibly weakening the
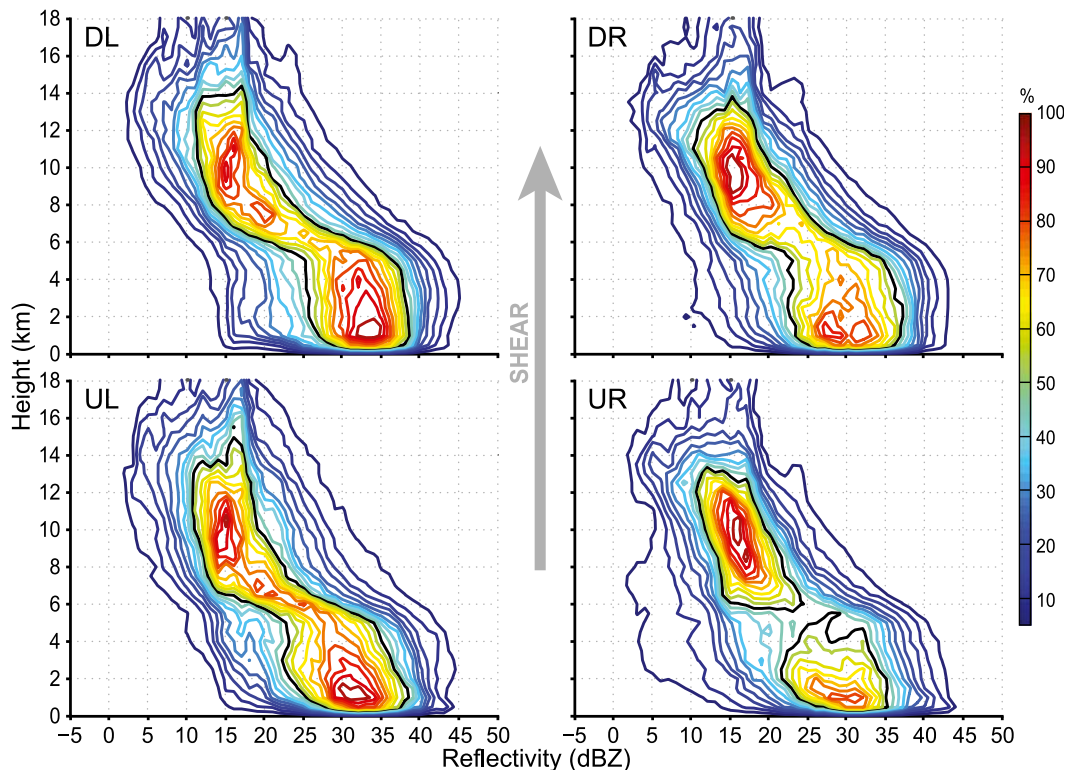
FIG. 2. As in Fig. 1, but separated according to shear quadrant. Quadrants are labeled DR, DL, UL, and UR.

upper-level frequency peak. Finally, the dataset used by Hence and Houze (2011) had considerable diversity of storm strength, whereas the dataset here skews toward more intense storms, possibly affecting the magnitudes of the low-level frequencies of occurrence.

Separating the total eyewall into shear-oriented quadrants highlights the structural differences around the storm. To ensure an appropriate comparison between quadrants, the CFADs are each normalized by their respective maximum frequency (Fig. 2). Many similarities to the total eyewall CFAD exist in each quadrant: the lower- and upper-level frequency maxima, brightband structure, and overall reflectivity range. However, closer examination of each quadrant reveals important structural differences. The two frequency peaks are nearly equally sharp in the left-of-shear quadrants, while the right-of-shear quadrants have far fewer intense low-level reflectivities; UR has the smallest amount. Furthermore, the modal values in the right of shear quadrants are centered on weaker reflectivities. This variation with shear is broadly consistent with that found by Hence and Houze (2011). The increased presence of low-level hydrometeors left of shear is consistent with the surface rainfall patterns seen in Chen et al. (2006) and the composite cross sections of Reasor et al. (2013).

Despite the tendency for the right-of-shear distributions to peak at higher altitudes and weaker reflectivities, at the expense of the low-level reflectivities, the low-level modal distribution DR is not as anemic as UR. Centered on 30 dBZ, the DR modal distribution spans approximately 15 dB and exhibits little reflectivity variation below the melting layer, where the 50% contour is nearly vertical. Intense reflectivities occur relatively frequently both near the surface and up to the melting layer; their vertical extent suggests convective generation and lifting by updrafts. In the transition to the DL quadrant, the structure changes, notably reflected by the increased frequencies below the melting layer. The low-level frequency maximum is strong DL. Moreover, the largest frequencies are centered on 33 dBZ and extend up from the surface through 6 km, while the 95% contour line spans 30–35 dBZ, not far above the surface. The vertically uniform frequency distribution below 6 km suggests the presence of updrafts DL, as in DR, while the near-surface frequency maximum of intense reflectivity suggests strong fallout. The relative widths of the modal distributions DR and DL are opposite to that seen by Hence and Houze (2011). These differences are likely due to a combination of differences in storm diversity and attenuation (and correction) of the TRMM PR and airborne radar. Despite these differences, the
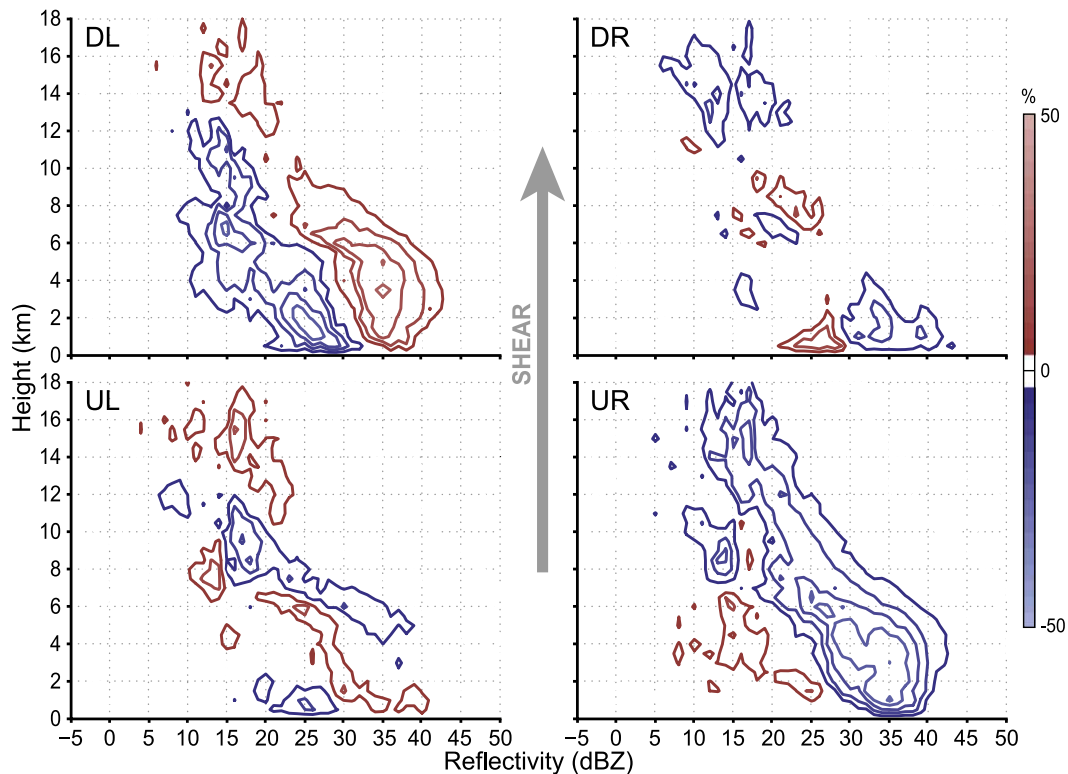
FIG. 3. Anomaly CFADs of reflectivity for each shear quadrant, where the CFAD in Fig. 1 has been subtracted from the CFADs in Fig. 2. Contours represent the frequency anomaly, contoured every 5%, where red contours are positive anomalies and blue contours are negative anomalies.

shift in relative importance of the upper- and lower-level frequency peaks is consistent.

A substantial structural change occurs in the upshear quadrants. While there is still a strong signature of copious amounts of intense reflectivities at low levels in UL, the frequencies drop off quite quickly with height. In particular, the modal distribution tilts toward weaker reflectivities with height, implying a reduction in lifting as strong precipitation still occurs closer to the surface. This tilt of the modal distribution is consistent with Hence and Houze (2011). The heavy near-surface rainfall generated downshear has been advected around the eyewall, and the remnants fall out in this quadrant (cf. Fig. 17 in Black et al. 2002). Finally, UR sees a dramatic reduction in convection. Very few intense reflectivities are found here and the modal distribution is not connected, implying weak upward motion.

These key structural differences are seen more clearly by removing the mean structure. We create anomaly CFADs by subtracting the total eyewall CFAD from the quadrant CFADs as shown in Fig. 3. In an effort to ensure our results are robust, we subsampled the data and recreated the anomaly CFADs. We selected, at random, one swath from each flight in order to generate the subsampled dataset; this was done five separate times. Overall, the subsampled data exhibited the same characteristics as the full dataset, signifying that structures in Fig. 3 are robust (not shown). This same technique was applied to all quadrant-separated figures throughout the study. The most striking feature of the anomaly plots is the strong departure from the total eyewall that prevails in the DL and UR quadrants. The distribution in DL shifts toward more intense reflectivities up through 18 km, whereas the strong negative anomalies UR signify a shift in the distribution toward weak reflectivities.

The deviations from the total eyewall are muted in the DR and UL quadrants. The low-level precipitation anomaly patterns yield further insight into the differing convective behavior of the DR and UL quadrants. Below 4 km and between 20 and 40 dBZ, the anomaly patterns of the two quadrants are opposite: there is a decrease in intense reflectivities and an increase in weaker reflectivities DR, while UL shows a slight preference for intense reflectivities and a reduction in weak reflectivities. In the layer from 4 to 6 km, the anomalous frequency pattern switches UL; reflectivities ranging from 30 to 40 dBZ are less common, whereas reflectivities weaker than 30 dBZ are more frequent. In contrast,
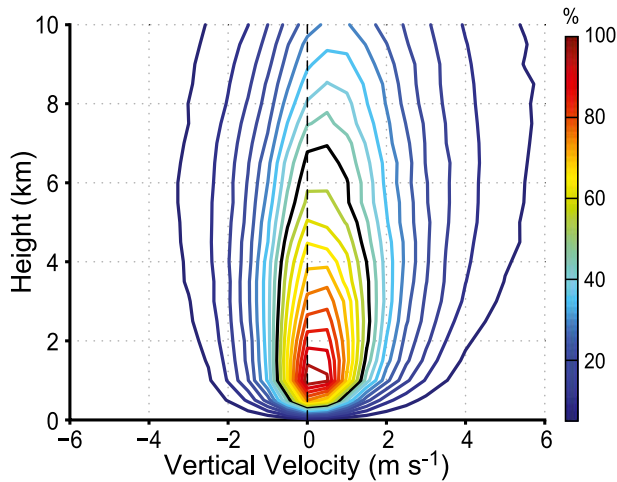
FIG. 4. As in Fig. 1, but for eyewall vertical velocity.

within this same layer, DR deviates little from the total CFAD. This distribution implies that larger particles may be more frequent UL, but they are constrained vertically to the lowest levels, again consistent with fallout. Low-level reflectivities still have an appreciable, if somewhat reduced, relative frequency DR that remains steady with altitude, indicating DR is a more favorable quadrant for upward motion than UL.

b. Vertical velocity

The previous discussion of the reflectivity CFADs establishes that the aircraft radar data are statistically consistent with the TRMM radar data studied by Hence and Houze (2011). With the Doppler-derived vertical velocity provided by the aircraft data and absent in the TRMM data, we may now test their hypotheses regarding how the nature of the inner-core convection varies from quadrant to quadrant relative to the environment shear vector. The eyewall vertical velocity statistics are displayed in Fig. 4. As expected, eyewall vertical motion is dominated by updrafts. The modal distribution spans a narrow range of weak velocities from -1 to $1.5\,\mathrm{m\,s^{-1}}$, and its vertical extent is rather shallow, again due to the decreasing number of scatterers aloft. The prevalence of weak motion has been noted in several observational studies (Jorgensen 1984; Black et al. 1996; Rogers et al. 2013). Nevertheless, outlier vertical velocities can be quite strong; the 0.5% frequency contour encompasses velocities between -6 and $+9\,\mathrm{m\,s^{-1}}$. As a consequence of the reduced spatial resolution, the outlier velocity magnitudes are weaker than those found in case studies by Black et al. (1996), Heymsfield et al. (2001), and Heymsfield et al. (2010). Although the strongest velocity magnitudes are more frequent above 4 km in Fig. 4, the aforementioned

studies found that updrafts maximize and strong downdrafts exist above 10 km, which we do not analyze because of degradation of data quality above this altitude. The tendency for the strongest inner-core convective-scale updrafts to occur above the melting level has been noted since the earliest use of airborne Doppler radar within tropical cyclones; Marks and Houze (1987) found the maximum vertical velocities in the eyewall of Hurricane Alicia (1983) at the 6–14-km levels and suggested that they were the result of release of latent heat of fusion, as had been indicated by the early modeling results of Lord et al. (1984). Drawing upon thermodynamic arguments, Zipser (2003) discussed how freezing heating is likely a general cause of the tendency for intense vertical velocities to occur at the highest levels in tropical convection. More specifically, observational studies by Black et al. (1996), Heymsfield et al. (2001), and Heymsfield et al. (2010) noted that the strongest updrafts are located above 8 km, maximizing in strength around 12 km in the latter study. Another recent modeling study of tropical convection by Fierro et al. (2009) produced a secondary updraft maximum between 10 and 12 km. In these studies, the secondary updraft peak is attributed to a combination of precipitation unloading at middle levels and additional buoyancy from ice processes farther aloft. Since we limit the vertical extent of our analysis to 10 km, because of the reduction in vertical velocity quality and availability above that altitude, we do not sample the uppermost updraft peak observed in these prior studies. Nonetheless, these studies also show an increase in vertical velocity beginning around 7 km, which our analysis captures.

As with reflectivity, separating the vertical velocity data into shear quadrants provides more insight about the asymmetric eyewall structure (Fig. 5). The differences between the upshear and downshear quadrants are striking and were robust when subsampled. As would be expected according to the analyses of Black et al. (2002) and Hence and Houze (2011), updrafts are found preferentially downshear, while downdrafts are more frequent upshear. Additionally, a strong wavenumber-1 asymmetry is visible in the frequency anomalies: DL and UR have weaker anomalies that are nearly identically opposite, while DR and UL have opposite patterns of stronger anomalies.

In the DR quadrant, the positive and negative frequency anomalies of updrafts and downdrafts indicate much more updraft activity and much less downdraft activity than in the eyewall as a whole. The 2% anomaly contour spans a wide range of updraft velocities, reaching a maximum updraft speed of $6\,\mathrm{m\,s^{-1}}$, while two smaller maxima of 10% straddle the $2\,\mathrm{m\,s^{-1}}$ line at 4 and 6 km. The negative anomalies, centered on $-1\,\mathrm{m\,s^{-1}}$, extend
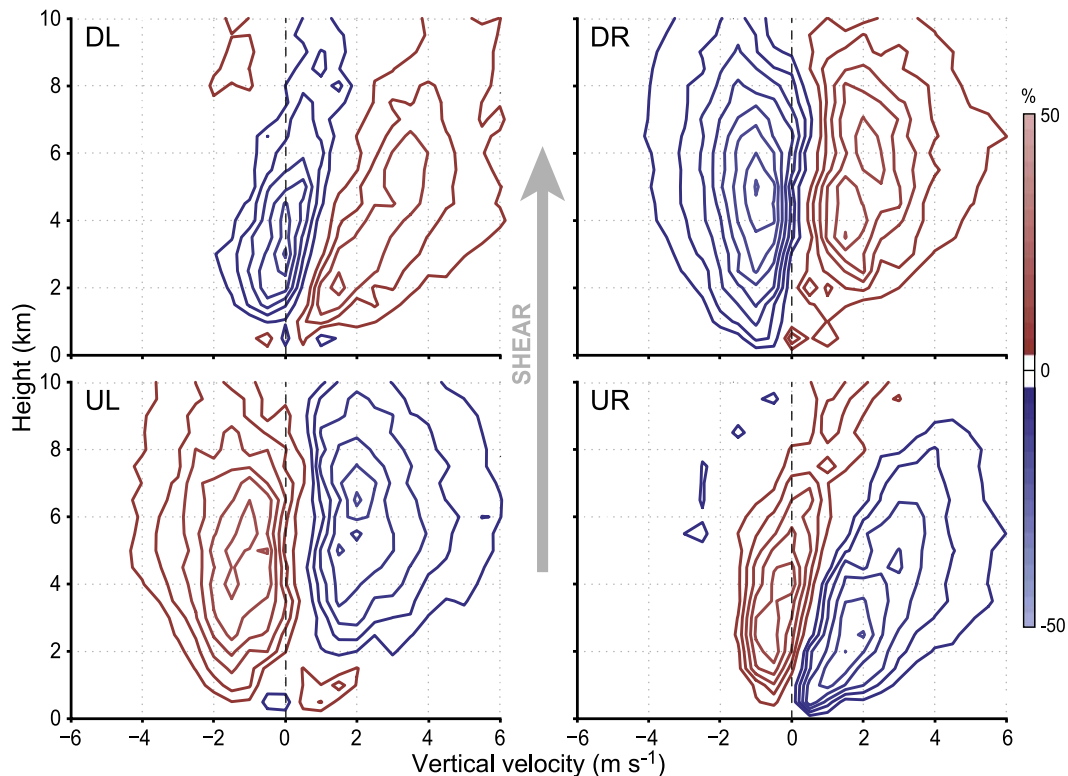
FIG. 5. Anomaly CFADs of vertical velocity for each shear quadrant, where the CFAD in Fig. 4 has been subtracted from the shear-separated CFADs (not shown). Contours represent the frequency anomaly, contoured every 2%, where red contours are positive anomalies and blue contours are negative anomalies.

from 1 to 10 km, and they are also stronger, maximizing at -16% for $-1\,\mathrm{m\,s}^{-1}$ and 5 km. This pattern of anomalies is consistent with convective initiation tending to occur in the DR quadrant: updrafts are beginning to occur here, but the convection has not yet reached the more mature stage in which downdrafts occur.

The frequency anomaly pattern DL is not a simple shift in the distribution. Similar to the DR quadrant, DL exhibits strong positive frequency anomalies of updrafts; however, the differences are noteworthy. The reduction in weak velocity frequency (i.e., $w \approx 0\,\mathrm{m\,s}^{-1}$) and the simultaneous increase in strong updraft frequency together indicate a broader distribution than that seen DR, with somewhat more frequent updrafts stronger than $4\,\mathrm{m\,s}^{-1}$. Yet, while positive anomalies DR more evenly cover a broad range of updraft intensities, the anomalies DL maximize for stronger updrafts. In addition, DL has fewer weak updrafts above 2 km; meaning upward motion that is present within DL is preferentially stronger. This occurrence of stronger drafts at higher altitudes is consistent with the results of Rogers et al. (2013), who found that convective bursts, defined in their study as vertical velocities greater than $5.5\,\mathrm{m\,s}^{-1}$

at 8 km (i.e., the top 1% of vertical velocities at that altitude), occur more often in the DL quadrant. Convection initiating DR, which matures and strengthens as it moves DL, has been noted previously in case studies by Black et al. (2002) and Heymsfield et al. (2001) and is consistent with simulations carried out by Frank and Ritchie (1999) and Braun et al. (2006).

Downdraft behavior also evolves through the quadrant transition. Negative frequency anomalies exist for downdrafts of all magnitudes and at all altitudes in the DR quadrant; downdrafts are not common. In contrast, negative frequency anomalies DL only surround weak downward motion below 5 km, and above 7 km only weak upward motion is less frequent. Outside of these negative anomalies, the weak downdraft frequency is nearly equal to the total eyewall above 6 km and may even be slightly greater. Though this presence of downdrafts pales in comparison to the positive anomalies of downdraft frequency UL, it does signify the tendency for downdrafts to develop in the transition from the DR to the DL quadrant in conjunction with the development of more mature and intense convection. In vertical cross sections shown in Black et al. (2002), strong updrafts left of shear were often flanked by
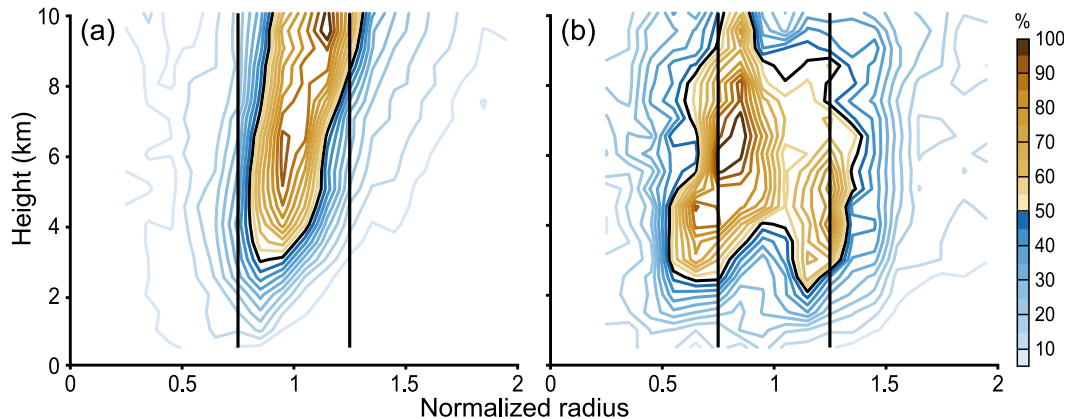
FIG. 6. Averaged joint probability distribution diagrams of radius and height for intense (a) updrafts ($w \geq 5\,\mathrm{m\,s^{-1}}$) and (b) downdrafts ($w \leq -4\,\mathrm{m\,s^{-1}}$). Normalized joint probability distribution diagrams were produced for each swath and then averaged to be representative of the entire dataset. Black lines denote the inner and outer edges of the eyewall.

downdrafts on either side, radially. Hurricane Bonnie, as analyzed by Heymsfield et al. (2001), also exhibited the development of a strong downdraft adjacent to convection at its peak intensity. Despite maximizing in the upper troposphere (10–15 km), this downdraft had considerable vertical extent down to an altitude of 7 km. Additionally, this distribution broadening likely contributes to the weakened composite vertical motion DL shown by Reasor et al. (2013); the strong updrafts and increasing number of downdrafts could cancel each other out in a composite analysis, particularly when considering eyewall variability from storm to storm.

In contrast to the updraft-dominated downshear quadrants, downdrafts become more prevalent upshear. Similar to the DR anomaly pattern, the distribution UL shifts toward downward motion. Moderate negative frequency anomalies are associated with updrafts of all magnitudes above 2 km. The distribution pattern UR is nearly the opposite of DL: positive frequency anomalies surround weak velocities (downdrafts below 5 km and updrafts above 7 km) and negative frequency anomalies surround moderate to strong updrafts. The combination of frequent weak vertical motion and infrequent updrafts indicates that the distribution is narrower than the total eyewall in the UR quadrant. The upshear quadrants are also broadly consistent with Reasor et al. (2013), though this analysis provides additional insight into how the mean motions are composed of updrafts and downdrafts. The composite vertical motion UL is reduced because of the increased presence of strong downdrafts cancelling out the updrafts that may still exist there as cells are advected around. The weak motion UR, on the other hand, is due to a narrow distribution centered on weak vertical velocities.

4. Intense vertical velocities

The possibility that strong local "bursts" of especially strong updraft motion may play a role in determining tropical cyclone intensity has received attention in the literature (e.g., Rogers et al. 2013). We therefore examine in this section the behavior of the outliers of the vertical velocity distribution in reference to the environmental wind. Specifically, we examine those data points with updrafts stronger than $+5\,\mathrm{m\,s^{-1}}$ or downdrafts stronger than $-4\,\mathrm{m\,s^{-1}}$. This updraft threshold is approximately equal to the convective burst definition in Rogers et al. (2013). To ensure that the outlier velocities are robust features, we require that they cover at least five contiguous pixels. Their horizontal and vertical characteristics are examined through radial–altitude joint probability distributions. However, since we are examining distribution outliers, the frequency counts are rather small. To prevent the distribution of a single swath from dominating the overall sample, we calculate a joint probability distribution of radius and altitude for each swath. Each distribution is normalized by its respective maximum count. We then take the average of the swath distributions, thereby creating a new distribution plot, which is subsequently normalized by its maximum value. Overall, the average distributions communicate the same result as the nonaveraged versions (not shown) but are more representative of the overall dataset.

Figure 6 shows the averaged distribution plots for the intense updrafts and downdrafts. The bulk of the strong updrafts reside within the previously defined eyewall band, though some do exist beyond those limits. They preferentially occur at middle to higher altitudes, specifically above 5 km. The increasing frequency of strong
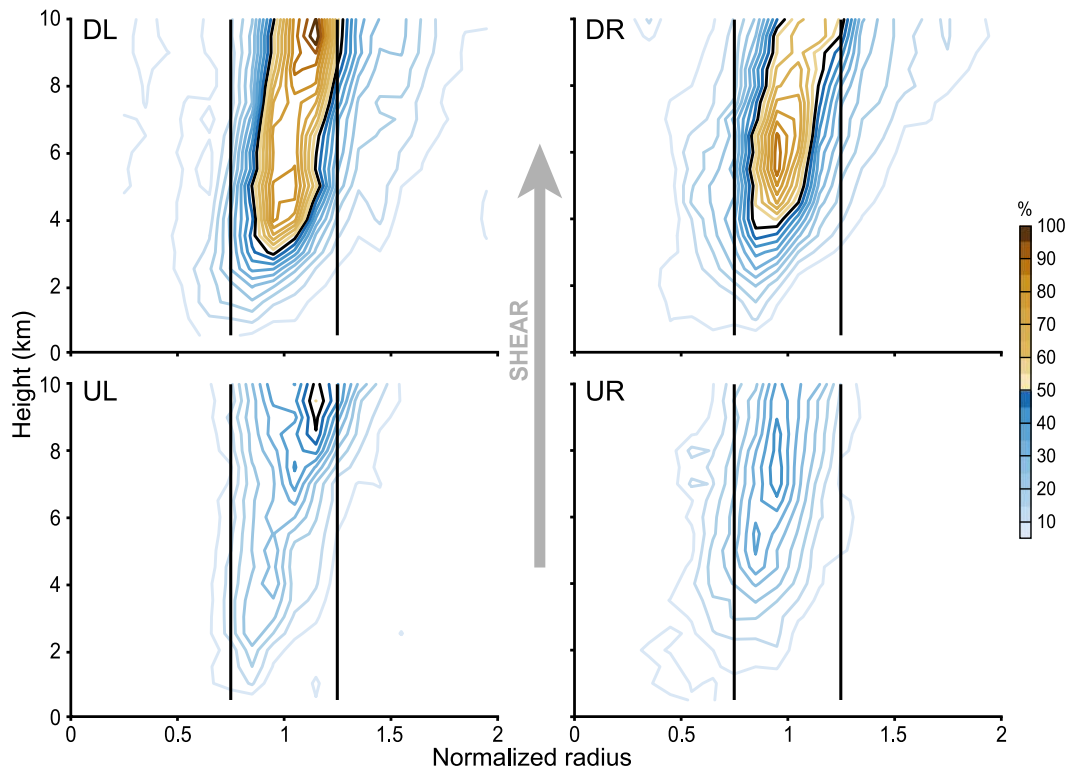
FIG. 7. As in Fig. 6, but for intense updrafts separated by shear-oriented quadrant. Joint probability distribution diagrams were produced for each quadrant and then normalized by the maximum frequency in any quadrant for each swath. These normalized quadrant diagrams were then averaged and normalized again by the maximum average frequency in any quadrant.

updrafts with altitude likely results from a combination of precipitation unloading and latent heat release from both freezing raindrops immediately above the melting level and cloud droplets higher aloft (Zipser 2003; Heymsfield et al. 2010). Strong downdrafts cover a larger radial range; however, two frequency maxima flank the edges of the defined eyewall band, straddling the location of the updraft frequency maximum, with the inner downdraft maximum being the larger of the two. In contrast to the strong updrafts, the strong downdraft frequencies peak at middle, rather than upper, levels. Hydrometeor weighting would more likely produce downdrafts at low levels where the reflectivity and rain rate are greatest. The concentration of downdrafts seen here higher aloft suggests that they are related to alternative mechanisms, such as the pressure gradient response to buoyancy or the shear-relative flow (Houze 1993, chapter 7; Yuter and Houze 1995; Bender 1997; Frank and Ritchie 1999; Didlake and Houze 2009). Another potential downdraft source is the detrainment of air within hot towers. In particular, in their analysis of Hurricane Bonnie, Heymsfield et al. (2001) highlight the existence of a large upper-level downdraft adjacent to an intense convective tower. They suggest the initial

development occurs in response to the overshooting top, which is then sustained and driven downward by evaporation of detraining air from the convective tower. Though this particular downdraft originates and maximizes above the vertical limit of our dataset, it is maintained down to an altitude of 7 km. Thus, this could play a role in the downdraft concentration seen in our data. However, the limitations of the tail-radar dataset prevent us from thoroughly evaluating this hypothesis.

Overall, the intense updrafts follow the same pattern with respect to shear as described in the previous section (Fig. 7). To highlight the quadrants that are the most favorable for the distribution outliers, we normalize each quadrant distribution by the maximum frequency occurring in any of the four quadrant distributions. Just as in the CFAD plots, these distributions were consistent when subsampled. The strongest updrafts occur preferentially downshear, with a slight preference for the DL quadrant. In the DR quadrant, the strong drafts occur most frequently in the midlevels, while they occur aloft in the DL quadrant. This progression could result from the maturation of convection as updraft cores rise helically around the eyewall. Since DR is the quadrant where convective initiation takes place, intense velocities
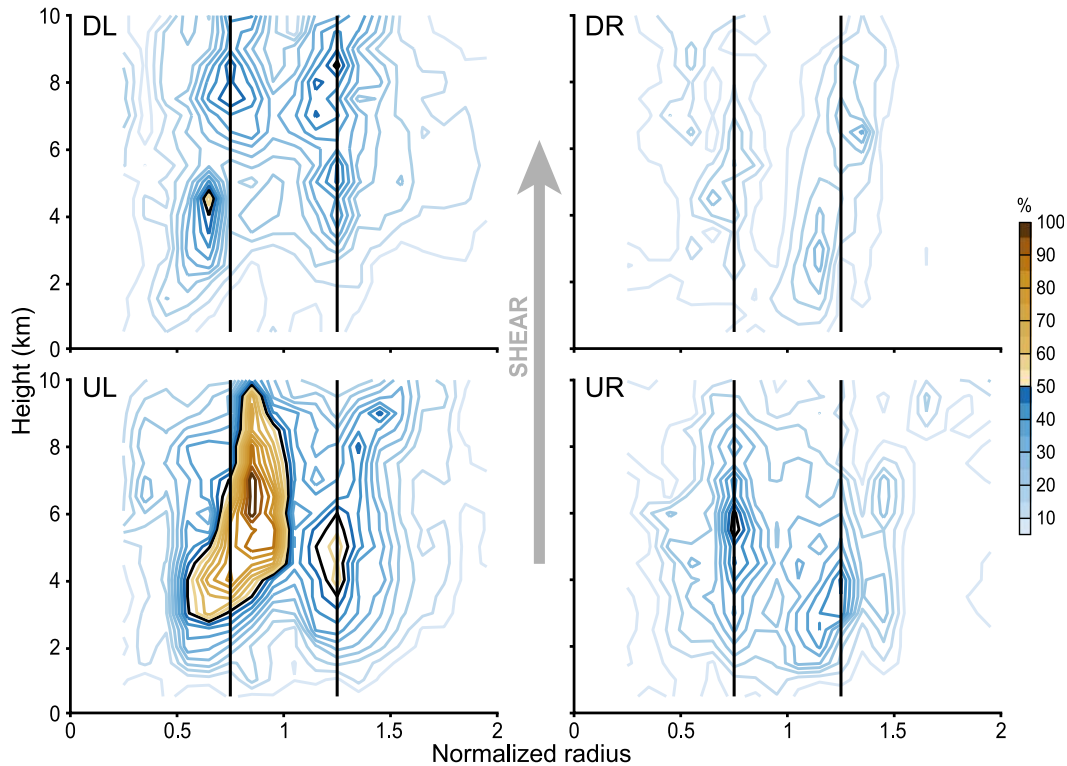
FIG. 8. As in Fig. 7, but for intense downdrafts.

may not have had sufficient time to strengthen. There is a steep reduction in strong updrafts in the upshear quadrants, where they only exist aloft.

Strong downdrafts also follow the same shear pattern as the weaker downdrafts; however, there is an unmistakable peak of intense downdrafts in the UL quadrant, which is robust when subsampled (Fig. 8). The DR quadrant, in contrast, has remarkably few intense downdrafts, which is unsurprising given its updraft-dominated structure as discussed in the previous section. Moderate amounts of intense downdrafts exist DL and UR, with the strong downdraft frequency DL peaking at midlevels and above 8 km and UR between 2 and 8 km. Strong downdrafts DL and UR concentrate along the edges of the eyewall. The midlevel maximum of downdraft occurrence DL strongly suggests that they may result from potential mechanisms such as dynamical forcing in response to the high-altitude convective updrafts or detraining air from the intense convection (Houze 1993, chapter 7; Yuter and Houze 1995; Bender 1997; Frank and Ritchie 1999; Heymsfield et al. 2001; Didlake and Houze 2009). The intense downdrafts UL maximize in frequency on the inner edge of the eyewall, which could at least partially be a result of the radar signal becoming too weak because of radar attenuation. Black et al. (2002) suggested that the convective cores

that were initiated downshear developed precipitation-driven downdrafts upon moving into the UL quadrant. However, they also noted an example where downdrafts UL appeared to have an upper-tropospheric origin. Since convection begins to die in this quadrant, it seems unlikely that the convective generation mechanisms would directly cause downdrafts to initiate here, though they could be residual. The shear-relative flow is more conducive for downdraft generation and could be a likely explanation.

5. Context of the drafts

To get a sense of the behavior of the strongest updrafts and downdrafts around the storm, we place them within the context of reflectivity and horizontal velocity. To capture the dominant structures, we consider only the powerful updrafts that lie within the defined eyewall band, that is, normalized radius values of 0.75–1.25. Upon identifying the azimuth corresponding to an intense draft, the pixels that lie within 2° on either side at all radii and altitudes are flagged. These pixels are then averaged to create radial–height cross sections. Only unique data points are included; even though strong drafts may lie next to each other, such that their flagged sectors would overlap, the data points are not included
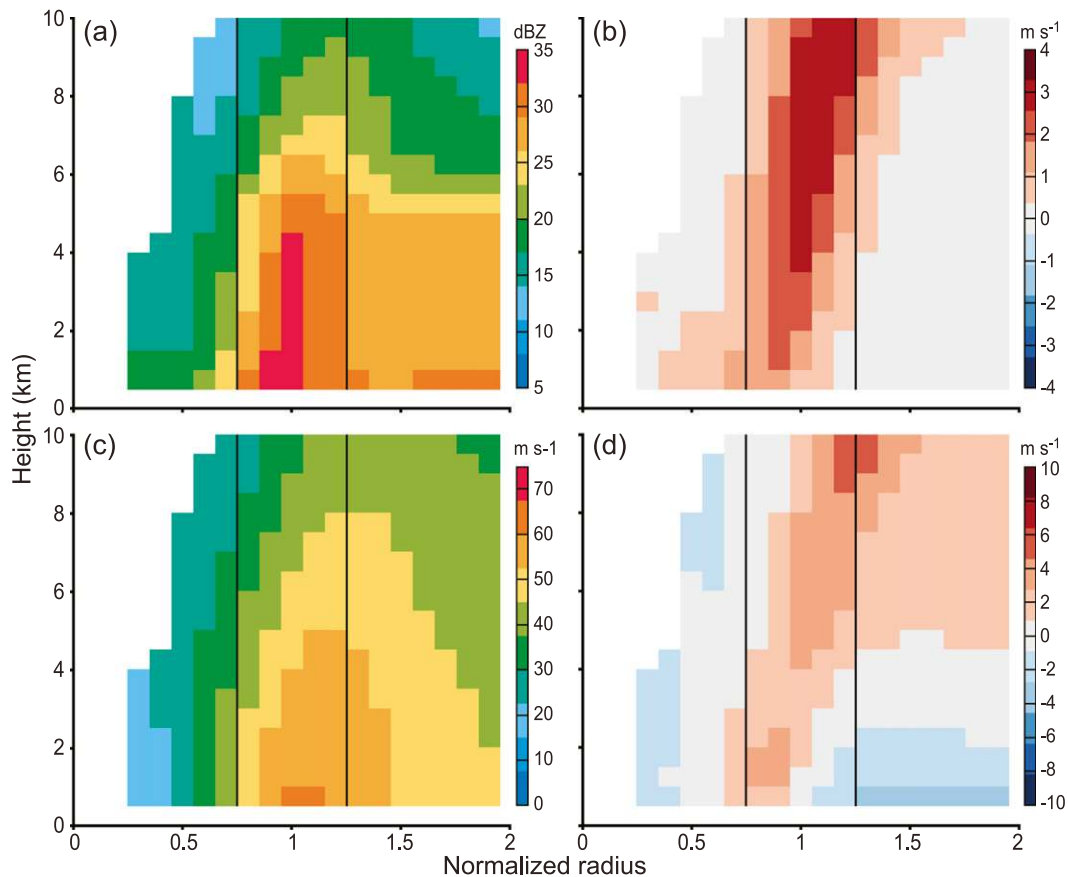
FIG. 9. Composite cross sections through intense updrafts of (a) reflectivity, (b) vertical velocity, (c) tangential velocity, and (d) radial velocity. Black lines denote the inner and outer edges of the eyewall.

multiple times. Figure 9 shows the mean eyewall radial–height structure in which the strong updrafts are embedded, requiring 50% of swaths to have data for a value to be plotted. Drawing upon the total storm structure, the reflectivity field associated with the vigorous updrafts is strongest within the eyewall, where lift, hydrometeor generation, and fallout are maximized. Similarly, the tangential wind field is centered on the radius of maximum wind, which exhibits the expected outward slope, with the peak values decreasing with altitude. The vertical velocity field is dominated by strong upward motion throughout 10 km, with the strongest upward motion occurring above the melting level. The accompanying radial flow displays the classic overturning secondary circulation. Low-level inflow of $-2\,\mathrm{m\,s^{-1}}$ below 2 km converges with $3\,\mathrm{m\,s^{-1}}$ outflow at the radius of maximum wind. Outflow dominates the structure above 3 km, reaching its maximum strength of $5\,\mathrm{m\,s^{-1}}$ on the outer edge of the strong composite updrafts.

To determine the context of the strong downdrafts, we follow the same procedure as for the strong updrafts; however, the radial range is larger (normalized radius

values between 0.5 and 1.5) to accommodate the different radial distribution seen in Fig. 6. While the reflectivity and tangential wind cross sections for strong downdrafts are slightly weaker than the corresponding plots for the strong updrafts, they nonetheless display a similar structure (Fig. 10). On the other hand, the vertical velocity cross section is marked by two regions of weak downward motion flanking an updraft centered on the radius of maximum wind. The updraft core is much weaker than that seen in the strong-updraft plot. However, the most distinctive difference between the updrafts and downdrafts occurs in the radial velocity cross section. The overturning circulation seen in Fig. 9 is nonexistent in the strong-downdraft composite. Outside the radius of maximum wind, with the exception of approximately $0\,\mathrm{m\,s^{-1}}$ radial flow between 0.5 and 1 km, the radial flow below 3 km is weakly outward. Above this outflow, the radial flow is weak, though slightly inward. A narrow filament of weakened outflow that strengthens above 8 km is concurrent with the composite updraft while weak inflow is collocated with the two regions of downward motion, as seen in Fig. 10b.
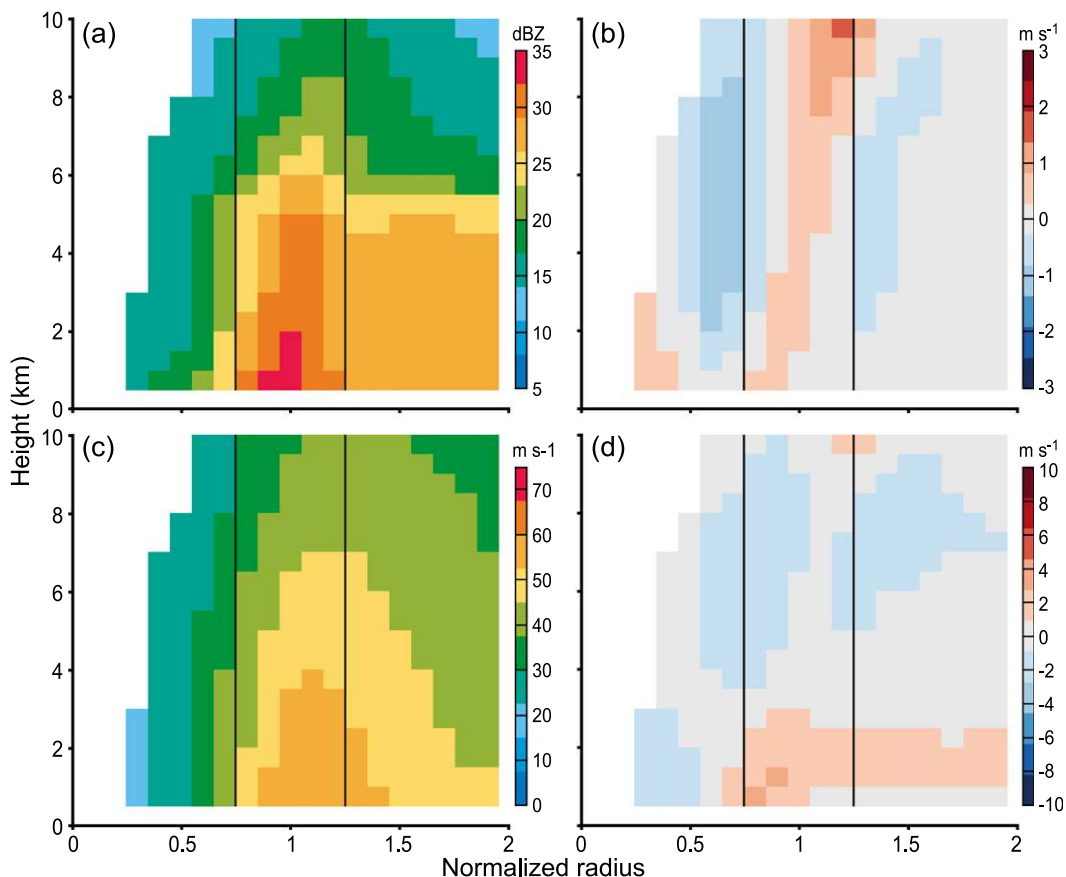
FIG. 10. As in Fig. 9, but for intense downdrafts.

While these overall composite cross sections suggest different behavior of the strong updrafts and downdrafts, further examination of Figs. 7 and 8 shows that the cross sections for these intense drafts are being drawn from nearly opposite quadrants of the storm (downshear quadrants for the updrafts and UL for the downdrafts). Thus, it is necessary to separate the analysis by shear quadrant. Since structural differences were most noticeable in the vertical velocity and radial velocity fields, the analysis will focus on these two variables. Table 2 shows the relative counts of strong vertical velocities in each quadrant. Since there is variability among the quadrants, particularly for the intense downdrafts, our analysis will focus on those quadrants with more comparable amounts.

The shear-separated cross sections for intense updrafts reveal that the vertical velocity behavior is relatively similar for each quadrant, despite the quadrant differences in updraft counts (Fig. 11). As in the total eyewall composite, strong updraft cores extend from the surface to 10 km and are constrained by the eyewall boundaries. The composite motion is strongest DR [similar to Reasor et al. (2013)], where it also occupies

the largest portion of the eyewall. Though DL has more powerful drafts, the composite updraft is weaker than DR, likely as a result of the increased presence of downdrafts that weaken the average vertical velocity magnitude. The updraft magnitude drops off even more UL, which has fewer updrafts and more downdrafts. UR shows a moderately strong composite updraft, despite this quadrant exhibiting some of the weakest updraft magnitudes overall. However, the structures UR exhibited more variability when subsampled, and the composite updraft strength is likely not robust.

The radial flow structure that accompanies strong updrafts is shown in Fig. 12. There is substantial variation among the quadrants, associated with the strong wavenumber-1 asymmetry of radial velocity, which is consistent with the results of Reasor et al. (2013). The strongest radial flow exists DR, where strong inflow on the order of $5\,\mathrm{m\,s^{-1}}$ lies below strong outflow of roughly $8\,\mathrm{m\,s^{-1}}$ outside of the radius of maximum wind. This pattern weakens substantially DL but has a similar structure, particularly outside the radius of maximum wind: near-surface inflow lies below a broad layer of outflow. A pronounced outflow region, corresponding to
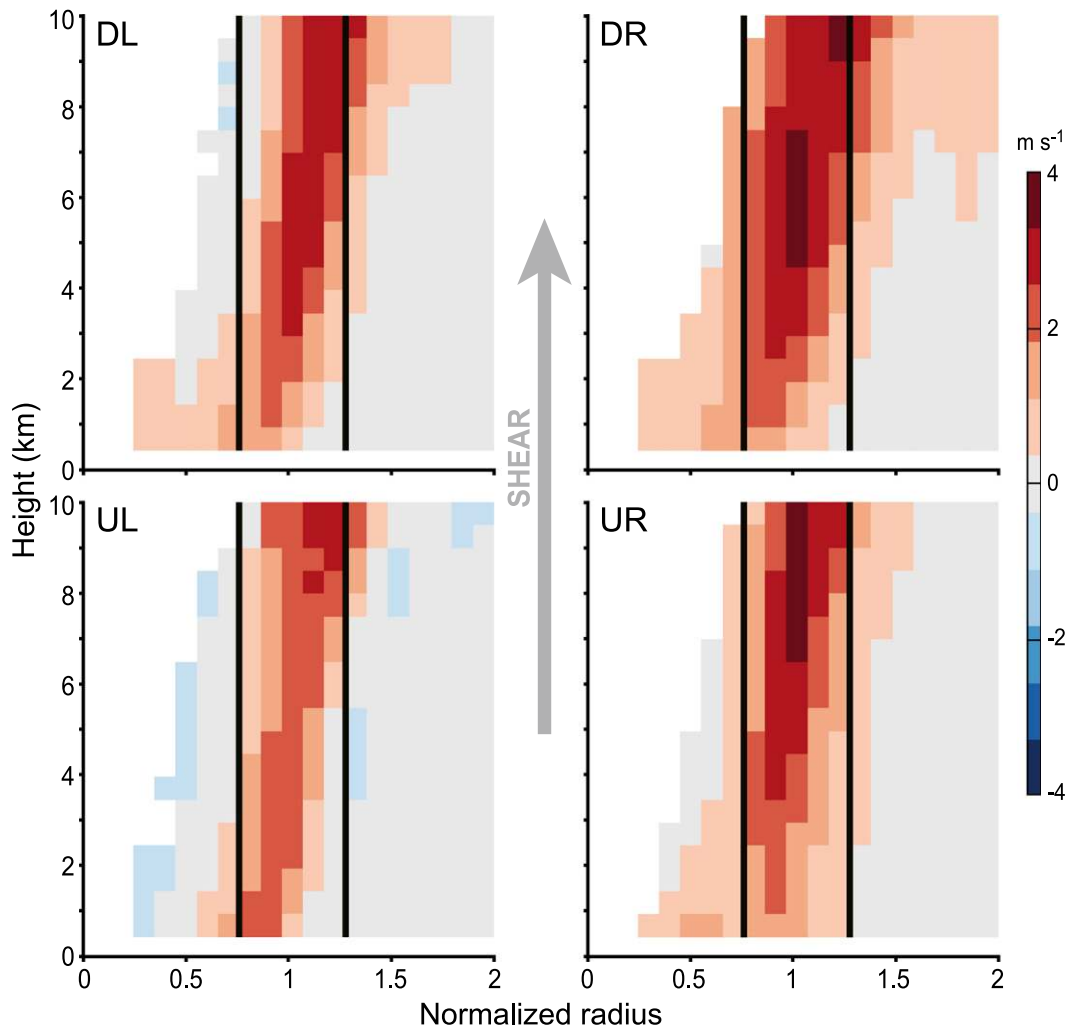
FIG. 11. Composite cross sections through intense updrafts of vertical velocity for each shear-oriented quadrant. Black lines denote the inner and outer edges of the eyewall.

the outward edge of the composite updraft seen in Fig. 11, slants radially outward with height DL from 1 km through 10 km. Additionally, there is a region of inflow on the radially inward flank of the composite updraft, this could be related to upper-level divergence associated with the strong updraft. Within the upshear quadrants, the expected low-level inflow and upper-level outflow pattern disappears; in fact, the radial flow is reversed UL. Outside of the radius of maximum wind, weak outflow exists below 5 km with inflow lying above it, though there is a shallow layer between 0.5 and 1 km where the radial flow is approximately $0\,\mathrm{m\,s^{-1}}$. Despite the reversal in the radial flow pattern, a thin filament of weak radial flow cuts through the stronger upper-level inflow UL. The weaker radial flow collocated with the outer edge of the composite updraft UL resembles a superposition of the radial flow associated with

a composite updraft (low-level inflow and upper-level outflow) onto the shear-relative background flow UR (low-level outflow and upper-level inflow). Corresponding to the decrease in intense updrafts in the UR quadrant, as indicated in Table 2, the pattern is less coherent. With the exception of the $5\,\mathrm{m\,s^{-1}}$ outflow core above 8 km, the composite radial velocities are relatively weak. Nevertheless, outflow in this quadrant resides

TABLE 2. Pixel counts of strong updrafts and downdrafts within each quadrant identified for cross-sectional analysis. Updrafts lie within normalized radius values of 0.75 and 1.25, while downdrafts lie within normalized radius values of 0.5 and 1.5.

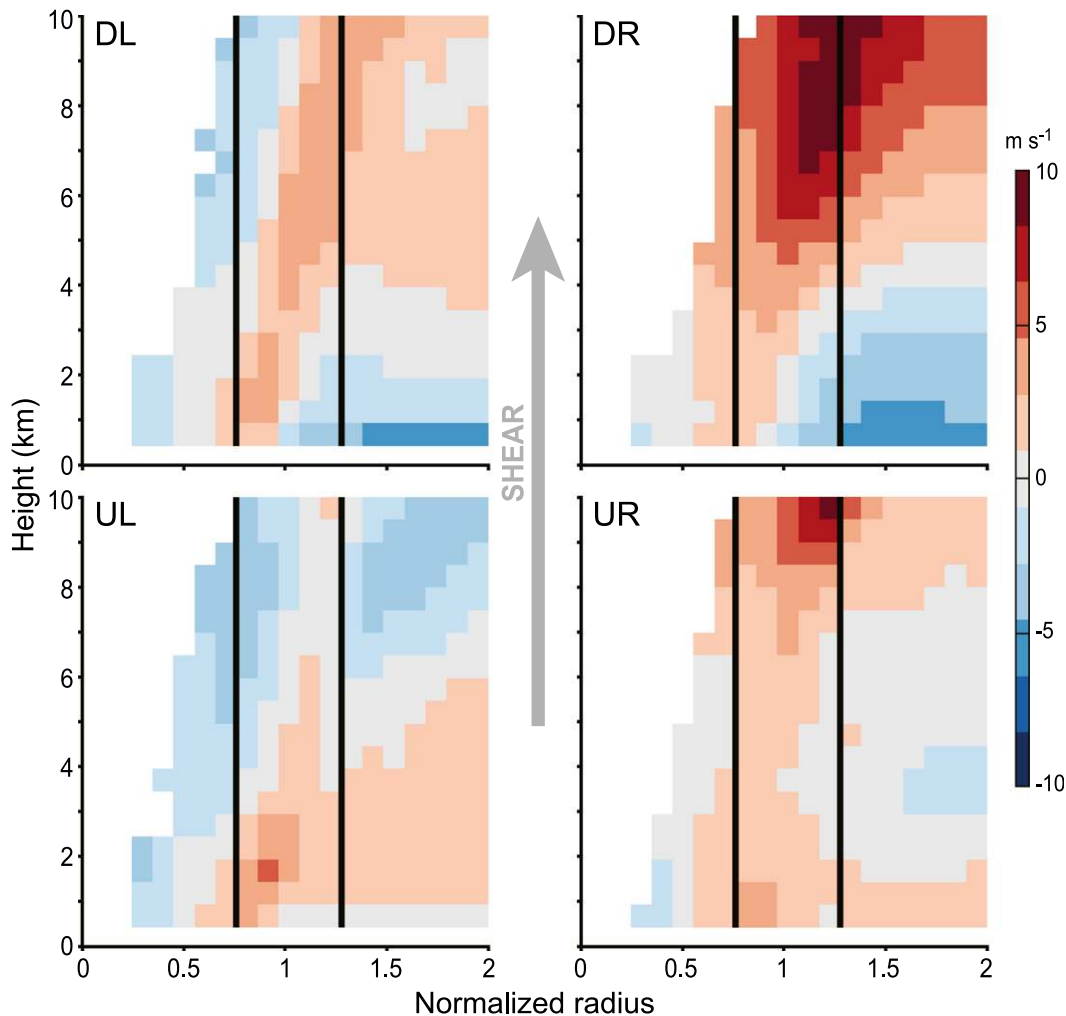|	DR	DL	UL	UR
Updrafts	12 984	15 523	6555	6096
Downdrafts	1688	3849	8193	5077

FIG. 12. As in Fig. 11, but for radial velocity.

within the eyewall, occupying the same radial–height space as the outer edge of the composite updraft UR in Fig. 11. However, this structure UR was not as consistent when subsampled, and when combined with the lack of intense downdrafts in this quadrant, it is not robust like the structures seen in the other quadrants.

Unlike their updraft counterparts, the intense downdrafts show considerable quadrant-to-quadrant structural variability in vertical velocity (Fig. 13). Updraft cores stretching from the surface to 10 km within the eyewall appear in the downshear quadrants, particularly DR, but are nearly absent upshear. Given the lack of downdrafts DR, as shown in Table 2, any structure is drowned out by the strong surrounding upward motion. The severe drop-off of intense downdraft frequency DR means structural differences in this quadrant may not be representative of the full dataset. Furthermore, the composite structure exhibited greater variability when

subsampled and is not significant. Thus, our analysis will focus on the quadrants with robust structures. Downdrafts hug each side of the updraft core and eyewall DL, though the interior one is stronger. Indeed, its magnitude is the strongest composite downward motion found in any quadrant, despite the greater downdraft frequency found in the UL quadrant (Fig. 8). Several factors could explain this structure, including the concentration of downdrafts along the eyewall edges DL in comparison to the large radial spread UL. The location of the strong downdrafts, especially in relation to upward motion, experiences more variability between the swaths UL. As a result, the structural diversity UL could result in features being averaged together, reducing the downdraft magnitude. Additionally, the contrasting structures of the downshear and UL composites explain the weak updraft seen in Fig. 8. The UL composite controls the total eyewall composite because of its downdraft-heavy
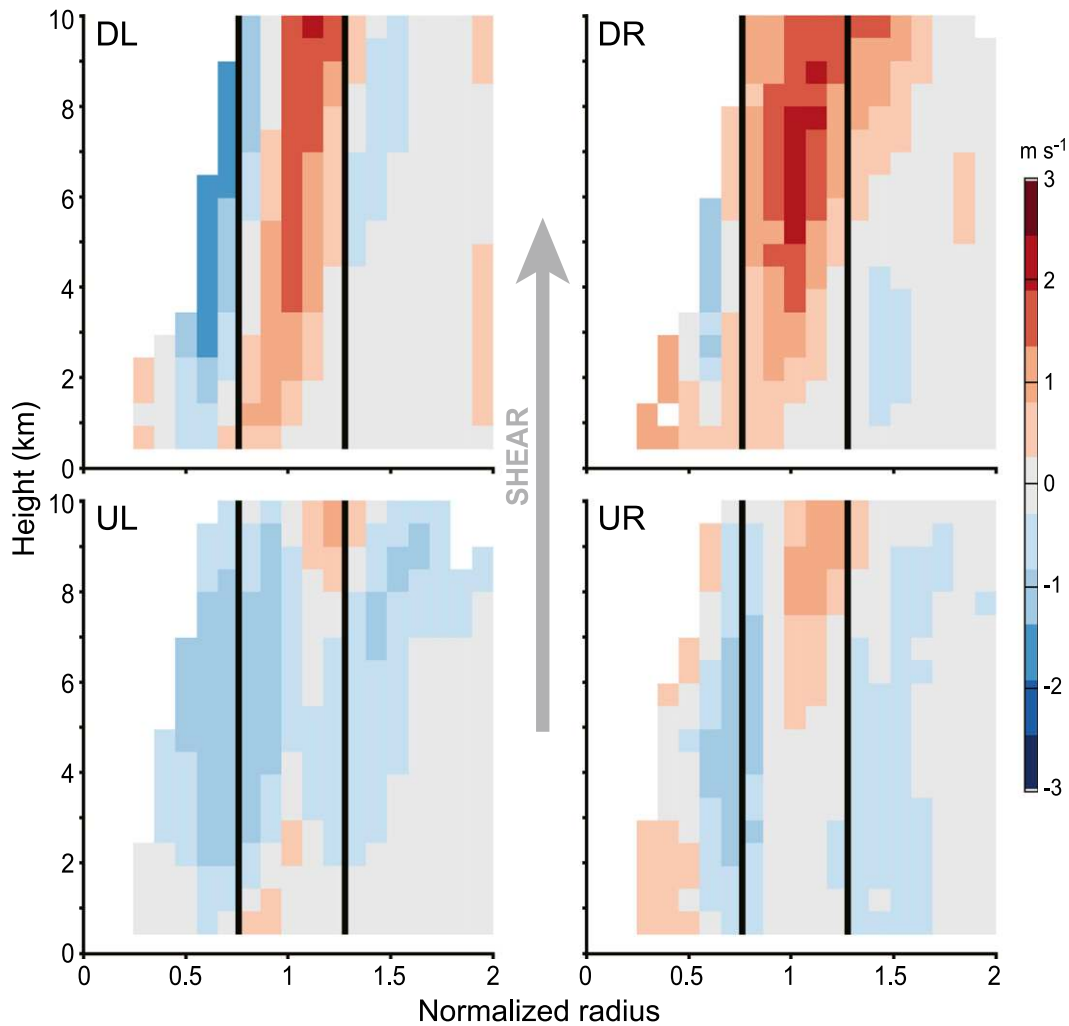
FIG. 13. Composite cross sections through intense downdrafts of vertical velocity for each shear-oriented quadrant. Black lines denote the inner and outer edges of the eyewall.

distribution, which negates the updrafts present in the downshear composites. Composite downward motion exists in two locations UL: a strong core inward of the radius of maximum wind between 2 and 9 km, and a weaker core outside the radius of maximum wind over the same altitude range. Upward motion is only present within the defined eyewall below 4 and above 8 km, and its magnitude is weaker. UR, the vertical motion is weak and disorganized. Similar to DR, the structure was not as consistent when subsampled, demonstrating that the composite structure UR is not significant.

The corresponding radial flow (Fig. 14) is similar to that for the strong updrafts, except for the notable absence of outflow tied to the updraft core in the left-of-shear quadrants (Fig. 12). The wavenumber-1 asymmetry emerges again, strongest in the DR and UL quadrants. The structure DR strongly resembles the corresponding

plot in Fig. 12, where inflow extends up to 4 km with strong outflow above it. Although this is the expected radial flow structure for this quadrant, the lack of samples DR, and variability when subsampled, indicate this structure is likely not significant. The overturning circulation is much weaker DL, especially when compared to the intense updraft radial flow in the same quadrant from Fig. 12. For the intense downdrafts, the inflow layer is restricted to the lowest 0.5 km of analysis and only reaches a maximum of $-2\,\mathrm{m\,s^{-1}}$ before converging with weak outflow at the radius of maximum wind. Outside the eyewall, outflow only extends up to approximately 6 km and strengthens to no more than $3\,\mathrm{m\,s^{-1}}$. Though there is a core of upward motion within the eyewall in Fig. 13, similar to the intense updrafts, there is no accompanying outward motion. Instead, weak inflow is present, particularly on the flanking edges of the
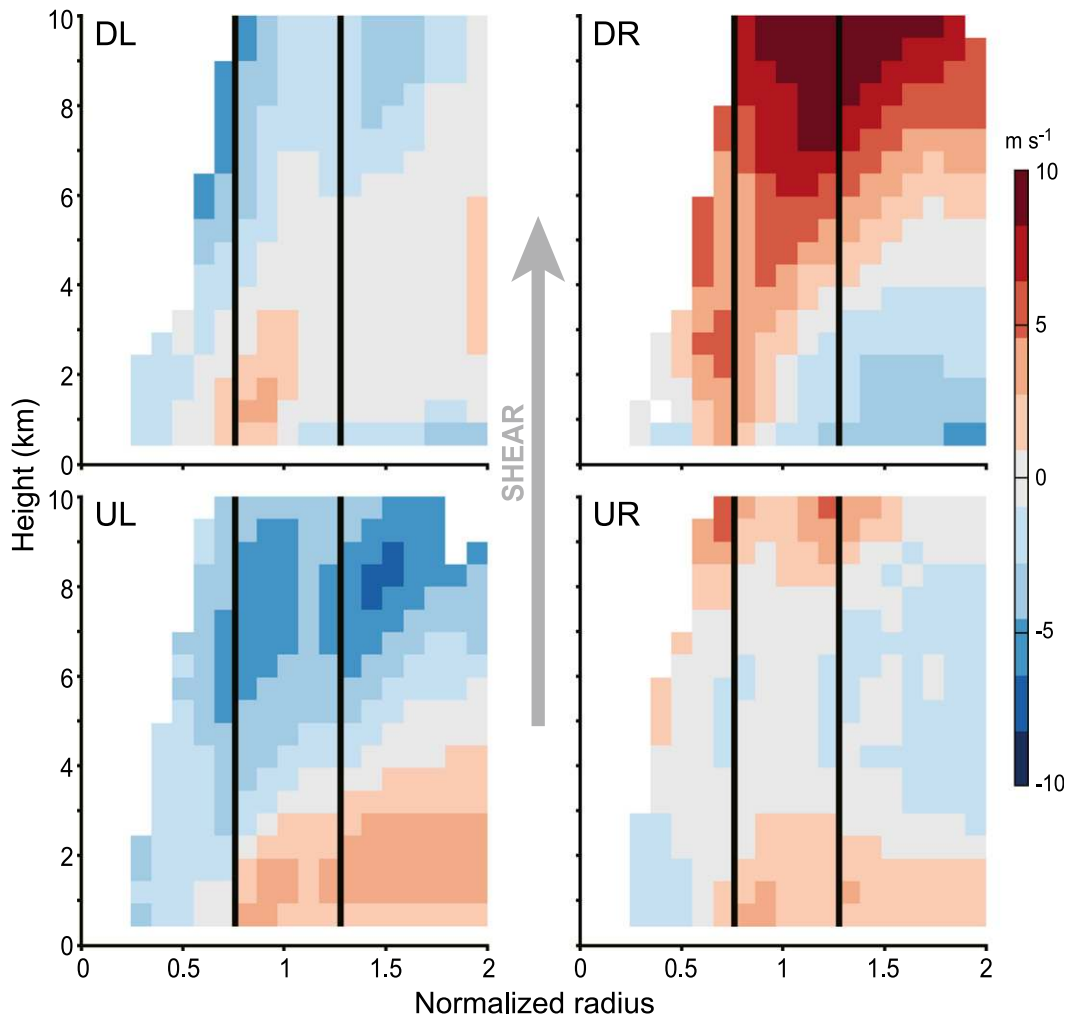
FIG. 14. As in Fig. 13, but for radial velocity.

updraft. UL is nearly the opposite of DR; moderate outflow below 3 km lies beneath relatively strong inflow. The upper-level inflow is stronger than that for the UL quadrant for strong updrafts. There may be a possible dynamical relationship between the downdrafts and radial flow pattern. More precisely, UL may be more favorable for downdrafts owing to upper-level inflow and/or from the possible entrainment of dryer midlevel environmental air. However, without thermodynamic data, we are unable to evaluate the latter mechanism. Similar to the vertical motion, the composite radial flow UR is weak and disorganized; it is not significant because of variability when subsampled, as mentioned for the vertical motion composite.

In summary, when comparing these radial flow cross sections for the intense updrafts and downdrafts, we see strong updrafts generally having stronger lower-level inflow and upper-level outflow, forming a stronger secondary circulation. Strong downdrafts, on the other

hand, exhibit the opposite pattern (stronger lower-level outflow and upper-level inflow). However, it is unclear whether the vertical motion is amplified by, or induces, the relative radial flow structure or if they arise from a common cause. Finally, the role of latent heat release and dry air entrainment in amplifying or weakening the vertical circulation cannot be fully explored without thermodynamic coverage.

6. Conclusions

We have analyzed airborne Doppler radar data from a large number of Atlantic tropical cyclones to study the frequency distributions of reflectivity and vertical velocity, and their variations with height, in the inner-core regions of tropical cyclones in the presence of shear. The velocity results are summarized in the schematic shown in Fig. 15. Our focus on the distributions extends the analysis of Hence and Houze (2011), whose statistical
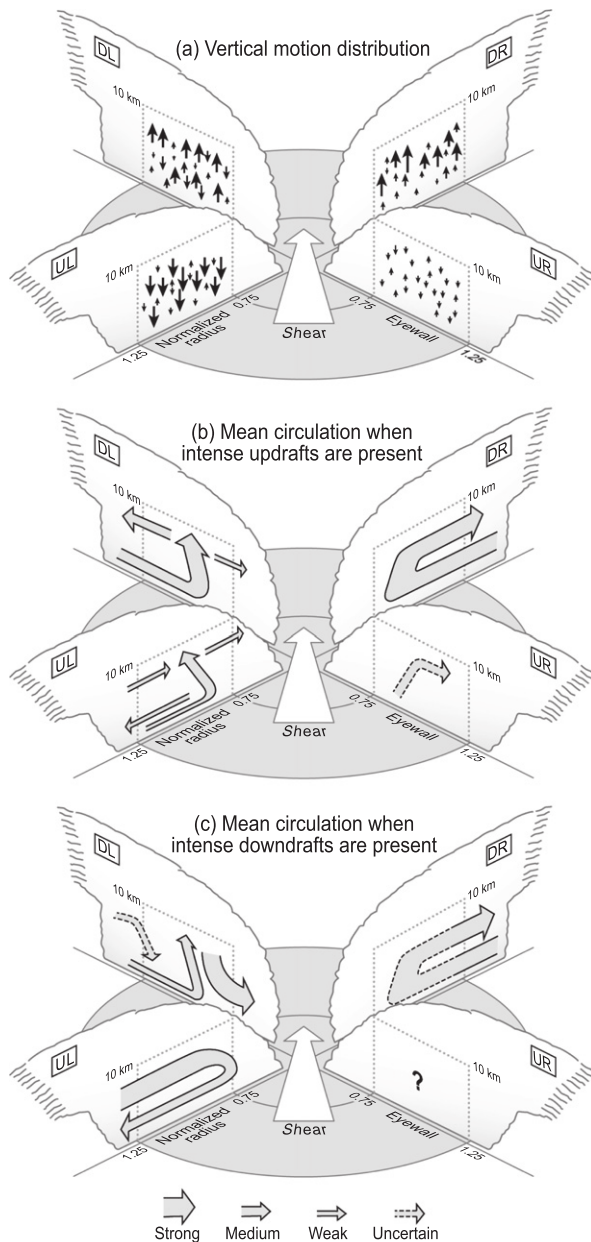
FIG. 15. (a) Three-dimensional schematic depicting the vertical motion distribution in each quadrant. The environmental shear vector is denoted by an arrow pointing toward the top of the figure, and quadrants are labeled according to their direction relative to the shear vector (DR, DL, UL, and UR). Concentric circles below the clouds show the locations of the eyewall (normalized radius values between 0.75 and 1.25), which connect to gray dashed boxes encompassing the eyewall up to 10-km altitude. Vertical arrows denote the vertical motion distribution, where size is proportional to magnitude. (b) As in (a), except illustrating the mean circulation that occurs when intense updrafts are present. Arrow width corresponds to composite velocity magnitude, as noted in the legend at the bottom. Dashed arrows refer to features that were present in the composite analysis but were shown to be not significant. (c) As in (b), except illustrating the mean circulation that occurs when intense downdrafts are present. The question mark denotes the structure existing UR is weak, disorganized, and not robust.

study was limited to reflectivity, which is the only parameter provided by the TRMM radar. The airborne Doppler radar data provided by Reasor et al. (2013) has allowed us to examine the velocity field along with the reflectivity so that we may test the hypotheses derived from reflectivity by Hence and Houze (2011).

The reflectivity distributions were broadly consistent with the TRMM data as analyzed by Hence and Houze (2011), despite the different sampling methods and sensitivities of the satellite and aircraft radars. The nearly constant downshear presence of strong reflectivities up to the melting layer signifies the influence of updrafts, while the increased frequency of stronger reflectivities from DR to DL suggests stronger, more mature convection DL. Strong reflectivities are present primarily at the lowest levels UL, because of fallout of larger hydrometeors that have been advected around the eyewall from downshear. The dearth of intense reflectivities UR indicates that the largest particles have mostly fallen out before reaching that quadrant and that initiation is generally not occurring there.

The statistical distributions of vertical velocity indicate a strong downshear–upshear difference in vertical motion, as shown in Fig. 15a. Since we have done a statistical analysis and not a case study analysis, we have represented the convective differences by arrow populations, where the length represents velocity magnitude. The distributions of arrows in the figure are meant to be visually consistent with convection initiating DR and maturing DL. Primarily upward motion occurs DR, with a mix of weak, moderate, and strong magnitudes. Updrafts are shown to be more powerful DL, particularly at upper levels, likely due to a combination of precipitation unloading and the release of latent heat of fusion. Updrafts weaken UL, before dying out almost entirely UR. Figure 15a therefore contains fewer upward arrows in the upshear quadrants and those that exist are of small magnitude.

Downdrafts also exhibit systematic behavior around the eyewall, as shown in Fig. 15a. The DR quadrant has the fewest downdrafts, while UL has the greatest number. In the transition from DR, where convection initiates, to DL, where the convection tends to mature, downdrafts become more prominent, developing primarily at higher levels, likely as a forced stable response to the strong, mature convective updrafts. Downdrafts do not appear frequently at lower levels, but attenuation of the radar beams cannot be ruled out as a possible explanation for the lack of low-level downdraft activity. This distribution analysis helps explain the reduced composite vertical motion DL found by Reasor et al. (2013) using a similar dataset; the increased number of downdrafts could cancel out the strong updrafts.

Deep-layer shear exhibits a similar influence on the patterns of occurrence of the most intense vertical velocities. Strong updrafts do not stray far from the eyewall and occur most often at upper levels, likely as a result of the release of latent heat of fusion (Zipser 2003) and precipitation unloading. They occur almost equally in the downshear quadrants, although with a slightly greater number DL. There is a steep dropoff in frequency within the upshear quadrants, but when strong drafts do occur, they appear in the upper levels. Strong downdrafts show a strong preference for UL and exist over a larger radial range. Downdrafts do occur DL and UR, but the frequency is far less and they tend to flank the edges of the eyewall.

Framing the powerful vertical motions within the context of radial flow reveals different mean dynamical behavior in the presence of intense updrafts and downdrafts. Figures 15b and 15c summarize the differing mean circulations found when intense updrafts or downdrafts are present, with the width of the arrows corresponding qualitatively to velocity magnitude. A strong overturning circulation exists DR. Though the shear-relative flow has diminished somewhat DL, denoted by moderate low-level inflow and upper-level outflow, an overturning circulation is nonetheless present near the strong composite updraft. The upper-level inflow on the inner edge of the eyewall could be a result of divergence near the top of the strong updraft. The radial flow pattern switches UL, and the resulting low-level outflow and upper-level inflow are rather weak. Weak radial flow breaks up the upper-level inflow just below 10 km, and the low-level outflow is reduced in the lowest layer of analysis: the overturning circulation associated with the moderately strong upward branch of the mean flow cuts through the upshear inflow–outflow pattern. Finally, though there is a hint of an overturning circulation UR, it was not significant, and a dashed arrow represents its uncertainty. In summary, strong updrafts are part of an overturning mean circulation, which is superimposed on whatever background flow is present.

A distinctly different mean circulation is present when strong downdrafts occur (Fig. 15c). Although the circulation DR matches what is expected from this quadrant based on the shear-relative flow, the inferred internal details were not statistically robust, so they are marked as uncertain. The secondary circulation does not appear DL; instead, a strong inward moving downdraft flanks the inner edge of an updraft, possibly in response to the strong convection in this quadrant. While there is a hint of an additional inward-moving downdraft on the outer flank, it is weaker and statistically uncertain. The radial flow is strongest UL, where the circulation is the opposite of DR. Finally, because of the weak velocities

and their variability when subsampled, the behavior UR is unknown and is denoted by a question mark. Overall, the mean circulation found when intense downdrafts are present is stronger outflow at low levels and inflow at upper levels. This updraft–downdraft structural difference is particularly noticeable UL, where the upper-level radial inflow is reduced substantially in the presence of the outflow accompanying the strong updrafts. It is not clear from this study whether the convective life cycle or the dynamic forcing (i.e., upper-level inflow) is critical in determining the UL downdraft concentration.

This study has shown that tropical cyclones can have significant asymmetries in both their precipitation and kinematic structure involving combinations of the mean horizontal and vertical flow. If future work (e.g., numerical modeling) reproduces the vertical velocity distributions and quadrant-varying mean circulations documented in this study, much could be learned about the mechanisms by which shear modulates vortex tilt and storm-relative flow in the inner-core regions of tropical cyclones. Future studies should aim for this objective. In addition, the effect of storm strength and size on the ability of shear to modify the inner-core structure cannot be ignored and should be investigated in future studies.

REFERENCES

Bender, M. A., 1997: The effect of relative flow on the asymmetric structure in the interior of hurricanes. *J. Atmos. Sci.,* **54,** 703–724, doi:10.1175/1520-0469(1997)054<0703:TEORFO>2.0.CO;2.

Black, M. L., R. W. Burpee, and F. D. Marks Jr., 1996: Vertical motion characteristics of tropical cyclones determined with airborne Doppler radial velocities. *J. Atmos. Sci.,* **53,** 1887–1909, doi:10.1175/1520-0469(1996)053<1887:VMCOTC>2.0.CO;2.

——, J. F. Gamache, F. D. Marks, C. E. Samsury, and H. E. Willoughby, 2002: Eastern Pacific Hurricanes Jimena of 1991 and Olivia of 1994: The effect of vertical shear on structure and intensity. *Mon. Wea. Rev.,* **130,** 2291–2312, doi:10.1175/1520-0493(2002)130<2291:EPHJOA>2.0.CO;2.

Braun, S. A., M. T. Montgomery, and Z. Pu, 2006: High-resolution simulation of Hurricane Bonnie (1998). Part I: The organization of eyewall vertical motion. *J. Atmos. Sci.,* **63,** 19–42, doi:10.1175/JAS3598.1.

Chen, S. Y. S., J. A. Knaff, and F. D. Marks, 2006: Effects of vertical wind shear and storm motion on tropical cyclone rainfall asymmetries deduced from TRMM. *Mon. Wea. Rev.,* **134,** 3190–3208, doi:10.1175/MWR3245.1.

Corbosiero, K. L., and J. Molinari, 2002: The effects of vertical wind shear on the distribution of convection in tropical cyclones. *Mon. Wea. Rev.,* **130,** 2110–2123, doi:10.1175/1520-0493(2002)130<2110: TEOVWS>2.0.CO;2.

——, and ——, 2003: The relationship between storm motion, vertical wind shear, and convective asymmetries in tropical cyclones. *J. Atmos. Sci.,* **60,** 366–376, doi:10.1175/1520-0469(2003)060<0366: TRBSMV>2.0.CO;2.

DeMaria, M., M. Mainelli, L. K. Shay, J. A. Knaff, and J. Kaplan, 2005: Further improvements to the Statistical Hurricane Intensity Prediction Scheme (SHIPS). *Wea. Forecasting,* **20,** 531–543, doi:10.1175/WAF862.1.

Didlake, A. C., Jr., and R. A. Houze Jr., 2009: Convective-scale downdrafts in the principal rainband of Hurricane Katrina (2005). *Mon. Wea. Rev.,* **137,** 3269–3293, doi:10.1175/2009MWR2827.1.

Fierro, A. O., J. M. Simpson, M. A. LeMone, J. M. Straka, and B. F. Smull, 2009: On how hot towers fuel the Hadley cell: An observational and modeling study of line-organized convection in the equatorial trough from TOGA COARE. *J. Atmos. Sci.,* **66,** 2730–2746, doi:10.1175/2009JAS3017.1.

Frank, W. M., and E. A. Ritchie, 1999: Effects of environmental flow upon tropical cyclone structure. *Mon. Wea. Rev.,* **127,** 2044–2061, doi:10.1175/1520-0493(1999)127<2044:EOEFUT>2.0.CO;2.

——, and ——, 2001: Effects of vertical wind shear on the intensity and structure of numerically simulated hurricanes. *Mon. Wea. Rev.,* **129,** 2249–2269, doi:10.1175/1520-0493(2001)129<2249: EOVWSO>2.0.CO;2.

Gamache, J. F., 1997: Evaluation of a fully three-dimensional variational Doppler analysis technique. Preprints, *28th Conf. on Radar Meteorology,* Austin, TX, Amer. Meteor. Soc., 422–423.

Hence, D. A., and R. A. Houze Jr., 2011: Vertical structure of hurricane eyewalls as seen by the TRMM Precipitation Radar. *J. Atmos. Sci.,* **68,** 1637–1652, doi:10.1175/2011JAS3578.1.

Heymsfield, G. M., J. B. Halverson, J. Simpson, L. Tian, and P. Bui, 2001: ER-2 Doppler radar (EDOP) investigations of the eyewall of Hurricane Bonnie during the Convection and Moisture Experiment-3. *J. Appl. Meteor.,* **40,** 1310–1330, doi:10.1175/1520-0450(2001)040<1310:EDRIOT>2.0.CO;2.

——, L. Tian, A. J. Heymsfield, L. Li, and S. Guimond, 2010: Characteristics of deep tropical and subtropical convection from nadir-viewing high-altitude airborne Doppler radar. *J. Atmos. Sci.,* **67,** 285–308, doi:10.1175/2009JAS3132.1.

Houze, R. A., Jr., 1993: *Cloud Dynamics.* Academic Press, 573 pp.

Jones, S. C., 1995: The evolution of vortices in vertical shear: Initially barotropic vortices. *Quart. J. Roy. Meteor. Soc.,* **121,** 821–851, doi:10.1002/qj.49712152406.

Jorgensen, D. P., 1984: Mesoscale and convective-scale characteristics of mature hurricanes. Part II: Inner core structure of Hurricane Allen (1980). *J. Atmos. Sci.,* **41,** 1287–1311, doi:10.1175/ 1520-0469(1984)041<1287:MACSCO>2.0.CO;2.

Lord, S. J., H. E. Willoughby, and J. M. Piotrowicz, 1984: Role of parameterized ice-phase microphysics in an axisymmetric, non-hydrostatic tropical cyclone model. *J. Atmos. Sci.,* **41,** 2836–2848, doi:10.1175/1520-0469(1984)041<2836:ROAPIP>2.0.CO;2.

Marks, F. D., Jr., and R. A. Houze Jr., 1987: Inner core structure of Hurricane Alicia from airborne Doppler radar observations. *J. Atmos. Sci.,* **44,** 1296–1317, doi:10.1175/ 1520-0469(1987)044<1296:ICSOHA>2.0.CO;2.

Nelder, J. A., and R. Mead, 1965: A simplex method for function minimization. *Comput. J.,* **7,** 308–313, doi:10.1093/comjnl/7.4.308.

Reasor, P. D., and M. D. Eastin, 2012: Rapidly intensifying Hurricane Guillermo (1997). Part II: Resilience in shear. *Mon. Wea. Rev.,* **140,** 425–444, doi:10.1175/MWR-D-11-00080.1.

——, M. Eastin, and J. F. Gamache, 2009: Rapidly intensifying Hurricane Guillermo (1997). Part I: Low-wavenumber structure and evolution. *Mon. Wea. Rev.,* **137,** 603–631, doi:10.1175/ 2008MWR2487.1.

——, R. Rogers, and S. Lorsolo, 2013: Environmental flow impacts on tropical cyclone structure diagnosed from airborne Doppler radar composites. *Mon. Wea. Rev.,* **141,** 2949–2969, doi:10.1175/MWR-D-12-00334.1.

Rogers, R. F., S. S. Chen, J. E. Tenerelli, and H. E. Willoughby, 2003: A numerical study of the impact of vertical shear on the distribution of rainfall in Hurricane Bonnie (1998). *Mon. Wea. Rev.,* **131,** 1577–1599, doi:10.1175/2546.1.

——, S. Lorsolo, P. Reasor, J. Gamache, and F. Marks, 2012: Multiscale analysis of tropical cyclone kinematic structure from airborne Doppler radar composites. *Mon. Wea. Rev.,* **140,** 77–99, doi:10.1175/MWR-D-10-05075.1.

——, P. Reasor, and S. Lorsolo, 2013: Airborne Doppler observations of the inner-core structural differences between intensifying and steady-state tropical cyclones. *Mon. Wea. Rev.,* **141,** 2970–2991, doi:10.1175/MWR-D-12-00357.1.

Wu, L., S. A. Braun, J. Halverson, and G. Heymsfield, 2006: A numerical study of Hurricane Erin (2001). Part I: Model verification and storm evolution. *J. Atmos. Sci.,* **63,** 65–86, doi:10.1175/JAS3597.1.

Yuter, S. E., and R. A. Houze Jr., 1995: Three-dimensional kinematic and microphysical evolution of Florida cumulonimbus. Part II: Frequency distributions of vertical velocity, reflectivity, and differential reflectivity. *Mon. Wea. Rev.,* **123,** 1941–1963, doi:10.1175/1520-0493(1995)123<1941: TDKAME>2.0.CO;2.

Zipser, E. J., 2003: Some views on "hot towers" after 50 years of tropical field programs and two years of TRMM data. *Meteor. Monogr.,* **29,** 49–49, doi:10.1175/0065-9401(2003)029<0049: CSVOHT>2.0.CO;2.